Real-Time Characterization of Uptake Kinetics of Glioblastoma vs. Astrocytes in 2D Cell Culture Using Microelectrode Array

Journal:	*Analyst*
Manuscript ID	AN-ART-06-2018-001198.R1
Article Type:	Paper
Date Submitted by the Author:	13-Aug-2018
Complete List of Authors:	Rivera, Jose; Purdue University, Electrical and Computer Engineering Sridharan, Siddarth; Purdue University, Electrical and Computer Engineering; Nolan, James; Purdue University, Agricultural and Biological Engineering Miloro, Stephen; Purdue University, Agricultural and Biological Engineering Alam, Muhammad; Purdue University, Electrical and Computer Engineering Rickus, Jenna; Purdue University, Janes, David; Purdue University, Electrical and Computer Engineering

SCHOLARONE™
Manuscripts

Journal Name

Real-Time Characterization of Uptake Kinetics of Glioblastoma vs. Astrocytes in 2D Cell Culture Using Microelectrode Array†

Jose F. Rivera,[‡,a,b] Siddarth V. Sridharan,[‡,a,b] James K. Nolan,[b,c] Stephen A. Miloro,[b,c] Muhammad A. Alam,[a,b] Jenna L. Rickus,[b,c] and David B. Janes[*a,b]

Extracellular measurement of uptake/release kinetics and associated concentration dependencies provides mechanistic insight into the underlying biochemical processes. Due to the recognized importance of preserving the natural diffusion processes within the local microenvironment, measurement approaches which provide uptake rate and local surface concentration of adherent cells in static media are needed. This paper reports a microelectrode array device and a methodology to measure uptake kinetics as a function of cell surface concentration in adherent 2D cell cultures in static fluids. The microelectrode array simultaneously measures local concentrations at five positions near the cell surface in order to map the time-dependent concentration profile which in turn enables determination of surface concentrations and uptake rates, via extrapolation to the cell plane. Hydrogen peroxide uptake by human astrocytes (normal) and glioblastoma multiforme (GBM43, cancer) was quantified for initial concentrations of 20 to 500 μM over time intervals of 4000 s. For both cell types, the overall uptake rate versus surface concentration relationships exhibited non-linear kinetics, well-described by a combination of linear and Michaelis-Menten mechanisms and in agreement with the literature. The GBM43 cells showed a higher uptake rate over the full range of concentrations, primarily due to a larger linear component. Diffusion-reaction models using the non-linear parameters and standard first-order relationships are compared. In comparison to results from typical volumetric measurements, the ability to extract both uptake rate and surface concentration in static media provides kinetic parameters that are better suited for developing reaction-diffusion models to adequately describe behavior in more complex culture/tissue geometries. The results also highlight the need for characterization of the uptake rate over a wider range of cell surface concentrations in order to evaluate the potential therapeutic role of hydrogen peroxide in cancerous cells.

1 Introduction

In studies involving uptake or release of selected extracellular analytes, determination of kinetic information is vital to move from phenomenological descriptions to mechanistic insight on fundamental cellular processes,[1] such as signaling[2–6] and metabolism.[7,8] Simultaneous measurement of uptake/release rates and concentrations at the cell surface has generally involved

[a] Electrical and Computer Engineering, Purdue University, West Lafayette, IN 47907, USA. E-mail: janes@purdue.edu

[b] Birck Nanotechnology Center, Purdue University, West Lafayette, IN 47907, USA.

[c] Agricultural and Biological Engineering, Purdue University, West Lafayette, IN 47907, USA.

‡ These authors contributed equally to this work.

† Electronic Supplementary Information (ESI) available: [details of any supplementary information available should be included here]. See DOI: 10.1039/b000000x/

adherent cell cultures in stirred fluid or suspended cells in static fluid. While these configurations can be characterized using volumetric approaches, the chemical microenvironment, which includes natural diffusion of chemical species, local depletion of consumed analytes, build-up of byproducts, and availability of cell-secreted soluble factors,[9–11] is altered by the stirring or the distributed nature of cells in suspension.[12] Approaches which better maintain the natural diffusion processes within the microenvironment, e.g., adherent 2D cell cultures in static media, can in principle account for the influence of the chemical microenvironment on the cell behavior. However, the relevant concentration in static media is the concentration at the cell surface, which can be significantly different from the concentration yielded by volumetric approaches. To address this problem, this paper presents time-resolved measurements of gradients and concentrations within few hundred of μm from adherent 2D cell cultures in static media

to simultaneously determine concentrations and uptake rates at the cell surface. The ability to simultaneously determine surface concentration and uptake rate can provide mechanistic insight beyond first-order reaction kinetics, enable development of more sophisticated diffusion-reaction models, and potentially help explain the differences in cell behavior in 2D versus 3D cultures.

As a representative example, as well as the focus of this paper, consider the cellular uptake of hydrogen peroxide (H_2O_2), a reactive oxygen species (ROS) that plays a vital role in the normal cell functioning when tightly regulated [6,13–16] and is associated to neurodegenerative diseases [17] and cancer onset [8] when dysregulated. The uptake rate of H_2O_2 (U_R), defined as the number of H_2O_2 molecules transported across the plasma membrane per unit time per cell (or per unit mass of protein), has been widely studied in bacterial, [18] fungal [5,19] and mammalian cells, [15,20–32] including brain cells such as neurons, astrocytes and glioma cells. Neurons have the highest glycolytic rate in brain and are a major producer of ROS, including H_2O_2, [33] but the cooperative coupling of neurons with astrocytes neutralizes H_2O_2. [20,34,35] Glioblastoma multiforme (GBM) is the most aggressive form of brain cancer, [36] originated from astrocytes [37] and, like astrocytes, express similar mechanisms to scavenge H_2O_2. [38] Maintenance of ROS levels in GBM is pivotal since high oxidative stress aids malignant progression but insufficient regulation results in cytotoxicity. [39] GBM reliance on antioxidant defenses to control metabolically-associated ROS, including H_2O_2, is a vulnerability which could be exploited therapeutically [8,40] and therefore has motivated the recent interest in characterization of H_2O_2 uptake rate of cancer vs. normal cells. [8,27,32,41,42]

While many studies on H_2O_2 uptake by various cell types have focused on the low concentration range where the uptake rate follows first-order kinetics, i.e., the uptake rate is proportional to the concentration, [15,20,22–27,43] other studies have extended the concentration range and found that uptake rate exhibits a non-linear dependence on concentration for various cell types, including astrocytes and glioma cells. [28–32] Separate determination of enzyme activities allowed this behavior to be ascribed to a combination of linear kinetics due to catalase (CAT) and Michaelis-Menten kinetics due to glutathione peroxidase (GPx1). [28–32] Since these observations were obtained with adherent cell cultures in stirred fluid, it is thus desirable to arrive at the same results but in static media.

Dynamic mapping of the concentration profile near the cell surface allows for determination of surface concentration (C_S) and surface gradient (G_S) by extrapolation to the cell plane. Surface uptake flux (F_S) is derived from G_S using Fick's law. Available fluorometric assays for extracellular H_2O_2 detection (see reviews [44–47]) have not been used to dynamically map concentration profiles. The most popular fluorometric assays, 10-acetyl-3,7-dihydroxyphenoxazine and boronate-based probes, are irreversible and therefore measure cumulative bulk effects rather than real-time local concentrations. [44,46,48,49] In contrast, electrochemical techniques like scanning electrochemical microscopy (SECM) [50–54] and self-referencing vibrating probe (SR) [55–61] can map concentration profiles perpendicular to the surface of 2D cell cultures [57,60,62] but are generally limited in terms of the overall measurement time required to obtain multi-point concentra-

tion measurements over relevant spatial scales, without perturbing the solution around the probe tip. [50,57–63] Electrochemical techniques based on microelectrode arrays (MEAs) [64–81] can provide real-time, customizable (in time and space) measurement capabilities and are more amenable to miniaturization, automation, and lab-on-a-chip integration, [77,82,83] which are desirable features for applications like point-of-care, microfluidic cell cultures, high-throughput drug screening, and space missions. MEAs have been generally utilized for 2D imaging of ex-vivo tissue and multi-point detection of cellular exocytotic release. Recently, MEA geometries and measurement approaches suitable for real time measurement of multi-point concentrations/gradients near aerobic granules and 2D cell cultures have been reported. [65,81]

In this study we have utilized a MEA-based approach to measure the time-dependent local concentration of H_2O_2 at multiple spatial locations near the surface of adherent 2D cell cultures of human astrocytes and glioblastoma multiforme (GBM43) cells in unstirred solutions. At each time point, the spatial profile is extrapolated to the cell plane to determine the corresponding C_S and G_S. Experiments over a range of initial concentrations (20-500 μM) allow determination of relationships between U_R and C_S. For both cell types, we found that the uptake rate is non-linear with the cell surface concentration, and this behavior is described by a combination of linear and Michaelis-Menten kinetic mechanisms, in agreement with observations from astrocytes and glioma cells from rat. [32] The obtained kinetic parameters describe the concentration dependence of the uptake rate and therefore can be used to refine reaction-diffusion models of antioxidant metabolism. Our results point to the need for characterization of U_R over a wider range of C_S whenever H_2O_2 plays a role as a therapeutic agent against cancer. Altogether, the MEA, methodology and experimental results constitute a proof-of-concept of on-chip characterization of H_2O_2 uptake kinetics of cancer vs. normal cells.

2 Experimental

2.1 Reagents

Human cerebral cortex astrocytes, astrocyte medium, cell freezing medium and 10 mg/ml poly-L-lysine were purchased from ScienCell Research Laboratories (Carlsbad, CA). Dulbecco's Modified Eagle's Medium (DMEM) and EDTA solution were purchased from Life Technologies (Carlsbad, CA). Astrocyte medium contained 500 ml of basal medium, 10 ml of fetal bovine serum (FBS, Cat. No. 0010), 5 ml of astrocyte growth supplement (AG_S, Cat. No. 1852) and 5 ml of penicillin/streptomycin solution (P/S, Cat. No. 0503). Glucose solution (50 ml of 200 g/L) and chambered coverglass systems with 1.0 borosilicate glass and 4-wells were purchased from Thermo Fisher Scientific (Waltham, MA). Hydrogen peroxide 30% (w/w) was purchased from Alfa Aesar (Ward Hill, MA) and phosphate buffer saline (PBS) pH 7.4 was purchased from Sigma-Aldrich (St. Louis, MO).

2.2 MEA design, fabrication and characterization

The 1D MEA array consists of five electrodes (10 μm $\times$ 10 μm) with inter-electrode separation of 140 μm center-to-center such

Table 1 List of symbols and units

Symbols	Definition and Units
$C(z,t)$	Concentration of H_2O_2 as a function of position z and time t (μM)
C_0	Initial concentration (μM)
C_S	Surface concentration (μM)
C_{bulk}	Concentration at the air/solution interface (μM)
G_S	Surface gradient ($\mu M\ \mu m^{-1}$)
F_S	Surface uptake flux (pmol cm^{-2} s^{-1})
U_R	Uptake rate (fmol s^{-1} cell^{-1})
k_F	Uptake rate factor, defined as the ratio U_R/C_S (L s^{-1} cell^{-1})
k_1	Rate constant of the linear kinetic mechanism (L s^{-1} cell^{-1})
J_0	Saturation rate of the Michaelis-Menten kinetic mechanism (fmol s^{-1} cell^{-1})
k_2	Concentration at $J_0/2$ (μM)
k_{obs}	Observed rate constant during volumetric sampling (s^{-1})
k_{cell}	k_{obs} normalized by the number of cells per unit volume of solution (L s^{-1} cell^{-1})
A	Culture area (cm^2)
N	Number of cells (cell)
V	Volume of solution (L)

that the spatial range of the gradient measurements is 560 μm (Fig. 1). Electrodes are located very close to the bottom edge of the silicon die and are designated E1, E2, E3, E4 and E5. Relative to the bottom edge of the die, E1 and E5 are the closest and the farthest electrodes, respectively. Fig. S-3† provides details of the microfabrication process. Platinum black was electrodeposited to increase the sensitivity of the electrodes, using reported protocols.[61,84] Electrodes were characterized for H_2O_2 response by performing cyclic voltammetry and amperometry in unstirred solution, finding sensitivity variations from electrode to electrode (21.8%) and from experiment to experiment (2.5%). The effects of these sensitivity variations are minimized via in situ transient calibrations where calibration factors are acquired immediately prior to the measurements near the cell surface.[81] No additional functionalization was required to achieve selectivity for H_2O_2 in the medium consisting of glucose and buffered inert electrolyte (phosphate buffer saline), a composition commonly found in the literature.[24,32,43,85–90] Control experiments (Fig. S-1†) showed that background signals measured for astrocytes and GBM43 in PBS/glucose (without H2O2) were smaller than the signal measured during exposure to 20 μM H_2O_2. The relative sensitivities of the electrodes to H_2O_2, glucose and lactate were also characterized (Fig. S-2†), and the selectivities of H_2O_2 with respect to glucose and lactate were found to be 1130 and 437, respectively. In general, changes in metabolic activity upon exposure to H_2O_2 would change the magnitude of background signals. Reports from the literature can be used to estimate the relative effects. The exposure of rat astrocytes to a sustained concentration of 50 μM H_2O_2 for 2 hours has been reported to reduce both glucose uptake and lactate release.[91] While some types of cancer cells release H_2O_2 due to oxidative stress,[92,93] no release of H_2O_2 by human glioblastoma cells has been observed upon exposure to H_2O_2.[94] Therefore, for cells in PBS/glucose with or without H_2O_2, the response due to cellular release of interferents (if any) is expected to be below the magnitude of the signals measured for H_2O_2, even for the smallest H_2O_2 concentration in this study.
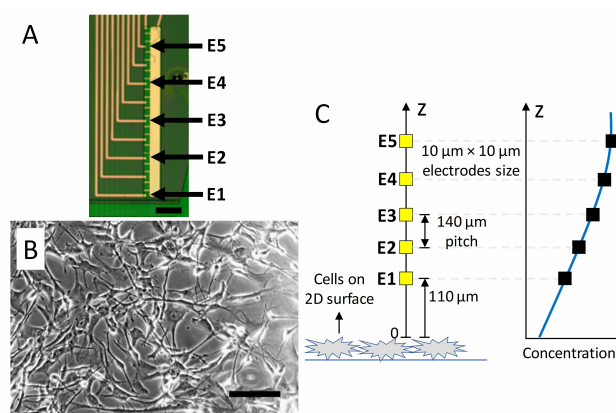
Fig. 1 MEA simultaneously measures concentrations at five positions near the surface of cells in 2D cell culture. (A) Photograph of a representative MEA. 10 platinum microelectrodes, 10 μm × 10 μm each, are arranged in a one-dimensional array, with the five electrodes indicated by arrows used in experiments, thus yielding a pitch of 140 μm. Scale bar is 100 μm. (B) Photograph of a representative culture of human astrocytes on a 2D surface. Scale bar is 100 μm. (C) Schematic of the experimental setup (not drawn to scale) illustrating how the five MEA electrodes acquire five spatial data points of the concentration profile near the cell surface. The MEA packaging allows positioning of E1 at 110 μm from the cell surface.

2.3 Apparatus and method for spatio-temporal resolution of gradients

The schematic diagram in Fig. 1(C) illustrates a reaction-diffusion system comprising a 2D cell culture (astrocytes or GBM43) surrounded by H_2O_2 solution and having five MEA electrodes arranged perpendicularly to the cell culture plane. Each electrode in the MEA operates amperometrically due to the application of a potential that drives the electrooxidation of H_2O_2 at the electrode surface and results in an electrical current proportional to the local concentration of H_2O_2. The MEA electrodes were individually addressed by dedicated potentiostats (Reference 600, Gamry Instruments Inc., Warminster, PA) using shared counter and reference electrodes. The counter electrode was a platinum wire of 0.5 mm diameter and the reference electrode was Ag/AgCl (sat'd 3M NaCl), both purchased from BASI Inc. (West Lafayette, IN). Un-

less stated otherwise, all potentials are referred to the Ag/AgCl (sat'd 3M NaCl) reference electrode, and all experiments were performed at room temperature. The 1D arrangement of the MEA electrodes allows mapping of the concentration profile over a spatial range of 560 μm. The sampling period of each electrode was set at 0.5 s. The measurements were run in a sequence of steps, as follows. Initially, no intentional H_2O_2 was in the culture medium. Upon exposure to H_2O_2 at t = 0 s, the cells immediately begin uptaking H_2O_2 and this uptake generates a transient concentration gradient in the direction perpendicular to the cell culture plane. As it is usual in amperometric measurements, the signals must be conditioned for some time such that the diffusion field around each electrode is reasonably stable. In the present study the conditioning time is 300 s and begins by biasing the electrodes 30 s after H_2O_2 exposure. During the conditioning time the MEA chip edge is at 5 mm from the cell surface, and just at the end of this conditioning time (i.e., at t = 330 s) the chip edge is positioned at 30 μm from the cell surface using a XYZ motion control system (Applicable Electronics, New Haven, CT). This movement of the MEA chip from 5 mm to 30 μm takes 4 s. The relevant data is thus acquired from t = 334 s onwards and the electrode closest to the cell surface (i.e., electrode E1) is located at 110 μm from the cell surface, as illustrated in Fig. 1. The amperometric signals measured at t = 330 s and the bulk initial concentration of H_2O_2 provided the information to compute the calibration factors for the electrodes, as reported elsewhere. [81]

2.4 Astrocyte cell culture

Human cerebral cortex astrocytes arrived from ScienCell (Carlsbad, CA) cryopreserved at passage one. Astrocytes were expanded and maintained according to the company's protocol. For each measurement of H_2O_2 consumption, passage-three astrocytes (5.0×10^4 cells cm^{-2}) were seeded onto poly-L-lysine-coated chambered coverglass 4-well systems and incubated for two days in a humidified atmosphere at 37 °C with 5% CO_2. Medium was replaced with fresh astrocyte medium one day after seeding. H_2O_2 uptake rate was measured after two days of incubation. By this time, cultures had grown to approximately 1.2×10^5 cells cm^{-2}. This number was calculated from a growth curve of three human astrocyte cultures (5.0×10^4 cells cm^{-2}) counted each day of incubation for three days. The doubling time was calculated to be 1.547 days. The exponential fit of the cell counts had an $R^2 > 0.99$. Cells were counted by hemocytometer and viability was determined through Trypan Blue Exclusion. Individual cell counts for each culture were acquired immediately following each measurement.

2.5 Glioblastoma cell culture

Primary patient-derived GBM43 cells were provided by Dr. Jann Sarkaria (Mayo Clinic, Rochester, MN) and have been described prior. [95] Cells were maintained in Dulbecco's Modified Eagle's Medium (DMEM) containing 10% fetal bovine serum in humidified atmosphere at 37 °C with 5% CO_2. Cells were propagated in T75 flasks and fed with growth media every other day. Cells were enzymatically dissociated using 0.25% trypsin/0.5 mmol

L^{-1} EDTA solution and passaged every 3 days. For each measurement of H_2O_2 uptake rate, propagated GBM43 cells were trypsinized and plated at a density of 10^5 in 1 mL of growth media in 12-well plates (Corning Costar 3515). H_2O_2 uptake rate was measured after the cells had grown to confluency over 3 to 4 days. Cells were counted by hemocytometer and viability was determined through Trypan Blue Exclusion. Individual cell counts for each culture were acquired immediately following each measurement.

2.6 Cell imaging and preparation for MEA measurements

Prior to exposing cultures to H_2O_2 and measuring uptake rate, cultures were imaged at 100X magnification with ToupView then washed twice with 5.5 mM glucose in PBS (pH 7.4). The culture wells were then filled with 0.3 ml (astrocytes) or 1 ml (GBM43) of 5.5 mM glucose in PBS. Next, the culture wells and MEA were put in position for measurement. Finally, 1.2 ml (astrocytes) or 2 ml (GBM43) of PBS with 5.5 mM glucose and H_2O_2 was added, so the resulting H_2O_2 concentrations were 20, 60, 100, 200, 300 or 500 μM in total volumes of 1.5 ml (astrocytes) or 3 ml (GBM43). The corresponding surface area and height of the liquid were 1.8 cm^2 and 0.83 cm (astrocytes), and 3.8 cm^2 and 0.79 cm (GBM43), respectively. Following each measurement in H_2O_2 solution, cells were imaged again. Fig. S-4† shows representative pictures of astrocyte and GBM43 cultures before and after exposure to 500 μM H_2O_2.

2.7 Viability assays

Live/dead assay of astrocyte and GBM43 was used to assess viability of cells after 2 hours of H_2O_2 exposure. Cultures were treated in one of four ways: (1) 2 hours in PBS with 5.5 mM glucose, (2) 2 hours in PBS with 5.5 mM glucose and 500 μM H_2O_2, (3) 20 minutes in formalin (negative control), and (4) directly assayed without treatment (positive control). Following treatment, cultures were stained with CellTracker Green (live stain) and propidium iodide (dead stain) (Thermo Fisher Scientific). Images were obtained using confocal fluorescence microscopy with model FV1000 (Olympus). Fig. S-5† shows the results. Two hours in 500 μM H_2O_2 had no apparent harmful effect on glioblastoma viability (Fig. S-5(H)†). On the other hand, two hours in H_2O_2 caused a fraction of astrocytes to lose adherence and thus being washed away during the live/dead assay, which would explain the apparent reduction in cell confluence (Fig. S-5(D)†). However, the astrocytes that remained adhered were viable.

2.8 Simulation details and numerical model

Since the concentration field induced by cellular uptake of H_2O_2 is one dimensional, i.e., perpendicular to the plane of cell culture, the simulation geometry consisted of a one-dimensional domain with length L equal to the distance between the cell surface and the solution/air interface, as shown in Fig. S-6†. The diffusion equation (1) is solved numerically using Comsol finite element software,

$$\frac{\partial C(z,t)}{\partial t} = D \frac{\partial^2 C(z,t)}{\partial z^2} \tag{1}$$

where $C(z,t)$ is the concentration of H_2O_2 as a function of position z and time t, and $D = 1.71 \times 10^{-9}$ m^2 s^{-1} is the diffusion coefficient of H_2O_2.[96] The boundary condition at the cell surface, located at $z = 0$, is set by U_R which is a function of C_S, as given by Eq. (2),

$$D\frac{A}{N}\left.\frac{\partial C(z,t)}{\partial z}\right|_{z=0} = U_R = k_F(C_S) \cdot C_S \qquad (2)$$

where A is the culture area and N is the number of cells. The C_S dependent uptake rate factor $k_F(C_S)$ is defined as the ratio U_R/C_S. As discussed in Section 3.4, the U_R vs. C_S relationship for each cell type is determined from experiments at multiple initial concentrations C_0, and $k_F(C_S)$ is expressed in units of L s^{-1} cell^{-1}. The boundary condition at the air/solution interface is set to zero flux, as given by Eq. (3).

$$D\left.\frac{\partial C(z,t)}{\partial z}\right|_{z=L} = 0 \qquad (3)$$

For each cell type, simulations were performed at the same values of C_0 used in the experiments, i.e., $C(z,0) = C_0$ where $C_0 = 20$, 60, 100, 200, 300 or 500 μM.

3 Results

### 3.1 Real time acquisition of transient concentrations at multiple positions from the cell surface

Fig. 2 shows representative concentration transients measured in real time at the electrode positions during experiments wherein the cell cultures of astrocytes and GBM43 are exposed to C_0 of 100 μM H_2O_2. Electrodes are labeled as E1 through E5, with E1 and E5 denoting the electrodes nearest to and farthest from the cell surface, respectively. These signals were acquired with sampling period of 0.5 s and were neither filtered nor averaged over time. Corresponding results for C_0 of 20, 60, 200, 300 and 500 μM H_2O_2 are included in Fig. S-7†. The relative values of the concentration amplitudes (E1 < E2 < E3 < E4 < E5) indicates the presence of a gradient in H_2O_2 concentration due to cellular uptake. The recorded concentration transients shown in Fig. 2 provide the information required to dynamically map the concentration profile of H_2O_2 and determine the corresponding uptake kinetics.

3.2 Mapping of the dynamic concentration profile from experimental data

Fig. 3 shows concentration as a function of distance from the cell surface at selected time points for both astrocytes and GBM43 cells exposed to C_0 of 100 μM H_2O_2. Solid symbols are experimental data points obtained from the MEA electrodes (E1-E5) at the indicated time points. The solid red lines represent fits at the corresponding time points, discussed later. Collectively, the data points indicate the evolution of $C(z,t)$ measured over a spatial scale of ~700 μm and for various time points between 360 and 4000 s. Although the concentration at each electrode was sampled every 0.5 s, as shown in Fig. 2, $C(z,t)$ is only shown for selected time points for the sake of clarity. Corresponding results for C_0 of 20, 60, 200, 300 and 500 μM H_2O_2 are included in Fig.

S-6†.

The uptake of H_2O_2 at the 2D cell surface depletes the analyte nearby and therefore induces a one-dimensional concentration gradient extending continuously into the bulk solution. Overall, the GBM43 cells exhibit higher H_2O_2 U_R than the astrocytes since the concentrations near the surface of GBM43 cells are smaller than those of astrocytes. While a nonlinear $C(z,t)$ was observed for both cell types at early times (0-500 s), non-linearity is more evident in GBM43 cells due to higher U_R. Beyond 500 s, the $C(z,t)$ over the spatial scale addressed is linear for both cell types.
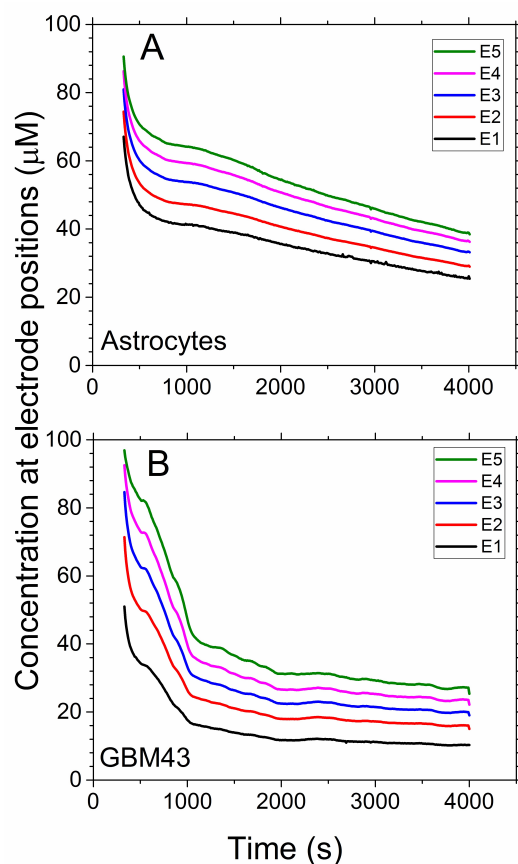
Fig. 2 Curves are representative measurements of local concentrations at the positions of the electrodes E1-E5 (located within 700 μm from the cell surface) for astrocytes (A) and GBM43 (B) exposed to C_0 of 100 μM H_2O_2. The sampling period is 0.5 s and no filtering nor moving-window averaging is performed on the acquired signals. A 330 s interval between addition of H_2O_2 (t = 0 s) and start of measurement allows stabilization of electrode response, and in-situ calibration technique described in text utilizes the current at each electrode at the end of that interval. The order in the amplitudes of the signals, E1 < E2 < E3 < E4 < E5, indicates the presence of a concentration gradient since E1 and E5 are the closest and farthest electrodes from the cell surface, respectively. Measurements were conducted with astrocytes and GBM43 cells at various initial concentrations, as described in text.

For each time point, C_S and G_S can be obtained via extrapolation of the concentration to $z = 0$ and calculation of the corresponding gradient, respectively. Considering the nonlinear $C(z,t)$ observed in the experimental points in Fig. 3, particularly at earlier time points, a simple linear extrapolation does not provide

accurate values for C_S and G_S. In order to provide an expression which better fits the experimental data and can be directly related to physical parameters, a general form of an expression describing a first-order irreversible reaction at a planar electrode in contact with a semi-infinite volume of solution[97] (see discussion and original expression in ESI†) was employed,

$$C(z) = A_1 \left[1 + A_2 erfc(A_3 z)\right] \quad (4)$$

where A_1, A_2 and A_3 are fitting parameters. Eq. (4) was used to fit the experimental concentration versus distance data at time points spaced by 10 s. Fig. 3 shows the fitted curves (solid red lines) corresponding to the experimental data sets presented in the figure. In the current study, the depth of the solution is finite and the 2D monolayer of cells is expected to act as H_2O_2 sink exhibiting kinetics beyond first-order; hence the fitting parameters A_1, A_2 and A_3 will have somewhat different but related physical interpretations from the original expression. The fitting was performed at each time point independently, without carrying any information over from prior time points, and the obtained best fits consistently provided $R^2 > 0.99$ at every time point for all the experiments: 36 experiments in total; 18 experiments for each cell type, comprising triplicates of 6 initial concentrations. The experimental results were also fitted by linear regressions (not shown), resulting in R^2 values within 0.79–0.95 and therefore confirming that fitting to a well-established diffusion-reaction model is better than simple linear regression.

3.3 Determination of surface concentration and gradient from experimental data

Once A_1, A_2 and A_3 are determined for a given time, the corresponding $C_S(t)$ and $G_S(t)$ can be obtained using expressions developed from Eq. (4), namely

$$C(z,t)|_{z=0} \equiv C_S(t) = A_1 + A_2 \quad (5)$$

$$\frac{\partial C(z,t)}{\partial z}\bigg|_{z=0} \equiv G_S(t) = -\frac{2A_2 A_3}{\sqrt{\pi}} \quad (6)$$

Curves of C_S and G_S versus time are determined using (5) and (6), respectively, for all the experiments performed in this study. The triplicate curves of C_S and G_S for each initial concentration are combined into averaged curves, and these averaged curves are indicated by solid lines in Figs. 4 and 5, respectively, for astrocytes and GBM43 cells exposed to C_0 of 20, 60, 100, 200, 300 and 500 μM H_2O_2. The error bars indicate standard deviation of the averaged curves (n = 3). The dashed lines in Figs. 4 and 5 represent the results of simulations for the corresponding C_0, discussed later. G_S is presented in units of μM μm^{-1} to facilitate physiological interpretations but other relevant units such as mol cm^{-4} can be obtained using appropriate conversion factors. Using the H_2O_2 diffusion coefficient from the literature,[96] the G_S values are converted into surface fluxes (F_S) as indicated by the corresponding scale in Fig. 5. Considering the whole spectrum of C_0 from 20 to 500 μM, astrocytes show less uptake than the GBM43 cells. Although both astrocytes and GBM43 cells showed changes in morphology after exposure to 300 and 500 μM H_2O_2 (see Fig.

S-4†), the cells kept consuming H_2O_2, highlighting the robust nature of the oxidant scavenging mechanisms present in both cell types. Separate live/dead stains (see Fig. S-5†) performed on the cells after exposure to 500 μM H_2O_2 indicated high viability of both cell types. The GBM43 cells exhibited better viability than astrocytes, suggesting that the cancerous cells are more resilient to H_2O_2 than their healthy counterparts. The dashed lines in Figs. 4 and 5 are simulated curves obtained from numerical solutions of the reaction-diffusion model (see Section 3.4) at the indicated C_0, using the geometry of the 2D cell culture and the kinetic parameters extracted from analysis of U_R as a function of C_S, as discussed in Section 3.5. It is important to note that only C_0 is modified from simulation to simulation, indicating that the diffusion model developed here qualitatively captures the physics of cellular uptake of H_2O_2 over the different time regimes and over the whole spectrum of C_0.
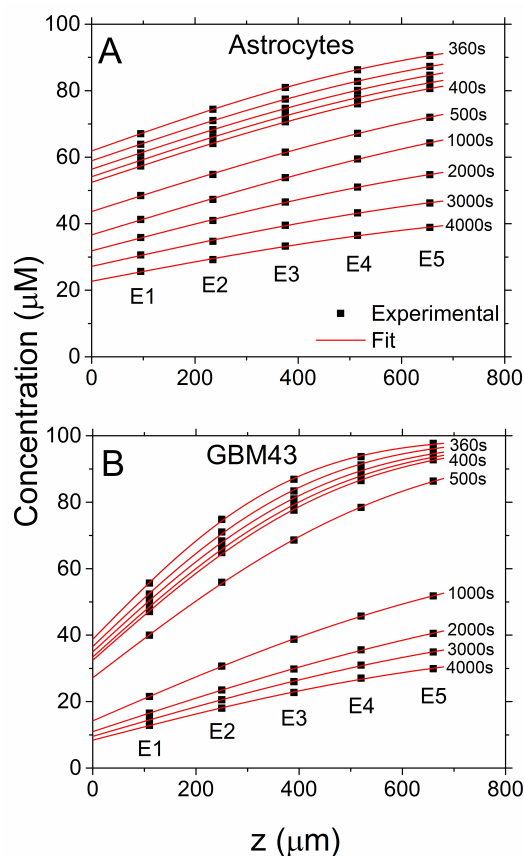
Fig. 3 Representative concentration profiles at the indicated time points, as measured by the electrodes E1-E5 (symbols) and as obtained from the best fits to a reaction-diffusion model (solid lines) for astrocytes (A) and GBM43 (B) exposed to C_0 of 100 μM H_2O_2. The procedure for the best fits and the reaction-diffusion model are described in the text. For clarity, the profiles are shown at relatively fewer time points as compared to the sampling time of 0.5 s. Concentration profiles within 360 and 400 s are shown in steps of 10 s. The data fits allow determination of surface concentration and surface gradient at each time point by extrapolation to the cell surface.
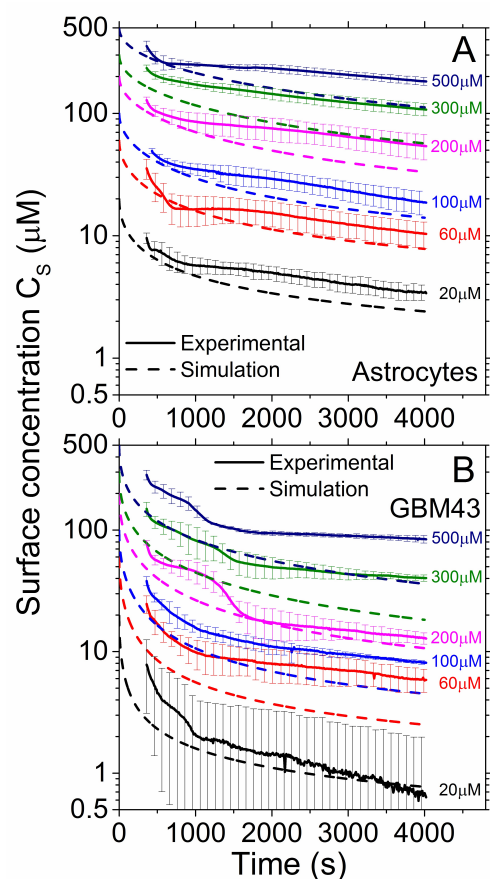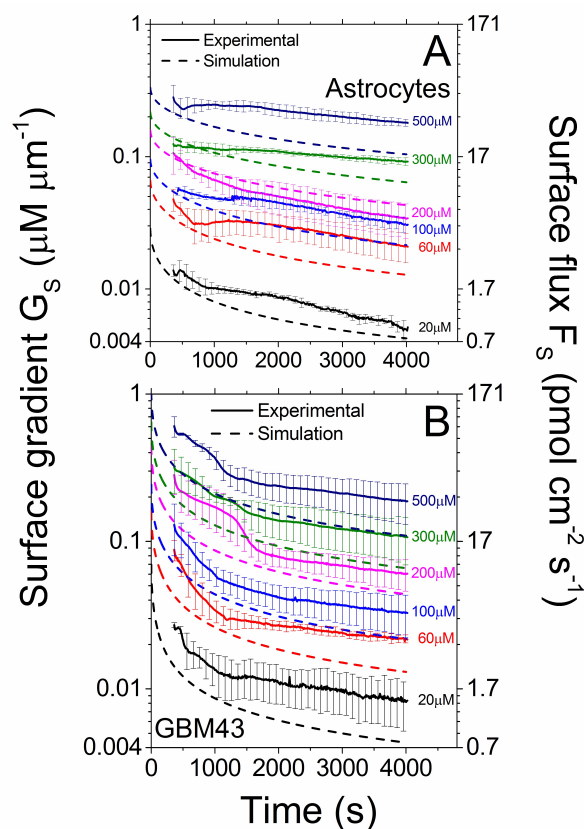
Fig. 4 Transient surface concentrations, C_S, for experiments with the indicated C_0 values for astrocytes (A) and GBM43 (B), as extrapolated from the concentration profiles fitted from experimental data (solid lines) and as obtained from simulations (dashed lines). Data points in solid lines are spaced by 10 s. Error bars indicate standard deviation of the mean value from triplicate experiments. For the sake of clarity, error bars are plotted every 100 s. The kinetic parameters (see Table 2) were kept fixed and only the initial concentrations were changed from simulation to simulation. Other simulation details are described in the text.

3.4 Real time determination of uptake kinetics and extraction of kinetic parameters

The transient behavior of C_S and G_S discussed above captures the effects of cellular kinetics in conjunction with the diffusion profile in the given geometry. In order to minimize variability in cell density between multiple experiments and extract the kinetic parameters in the same units as standard volumetric rate constants (see Discussion), the F_S (mol cm^{-2} s^{-1}) presented in Fig. 5 is normalized to the cell density (cell cm^{-2}) to obtain U_R on a per cell basis (mol s^{-1} cell^{-1}).

Open symbols in Figs. 6 and 7 indicate the values of U_R versus C_S extracted from experimental data for astrocytes and GBM43; both figures present the same data but over different ranges of C_S to help visualize some details in the U_R–C_S relationship. For each cell type, data is plotted for the various C_0 values in order to span the whole spectrum of concentrations for both cell types. This yields a series of overlapping segments (e.g. within astrocyte data, segments corresponding to C_0 of 300 and 500

μM correspond to segments covering C_S ranges of $\sim$110-240 μM and $\sim$175-350 μM, respectively). Shaded bands surrounding the open symbols indicate standard deviation of the mean value of U_R (n = 3). Overall, the U_R–C_S relationships are observed to be non-linear.

Fig. 5 Transient surface gradients, G_S, for experiments with the indicated C_0 for astrocytes (A) and GBM43 (B), as extrapolated from the concentration profiles fitted from experimental data (solid lines) and as obtained from simulations (dashed lines). The corresponding surface flux, F_S, (right axis) is computed as the product of G_S and diffusion coefficient of H_2O_2. Data points in solid lines are spaced by 10 s. Error bars indicate standard deviation of the mean value from triplicate experiments. For clarity, error bars are plotted every 100 s. The kinetic parameters (see Table 2) were kept fixed and only the initial concentrations were changed from simulation to simulation. Other simulation details are described in the text.

The solid lines passing through the experimental data points (open symbols) in Figs. 6 and 7 are best fits to Eq. (7), which describes the dependence of U_R on C_S using established kinetic mechanisms, namely linear (first term) and Michaelis-Menten (MM) [98,99] (second term),

$$U_R(C_S) = k_F(C_S) \cdot C_S = \left[k_1 + \frac{J_0}{k_2 + C_S} \right] \cdot C_S \qquad (7)$$

where k_1 is the rate constant of the linear mechanism, J_0 is the saturation uptake rate of the MM mechanism and k_2 is the MM constant (i.e., concentration at $J_0/2$). Note that the term in the brackets in Eq. (7) is the definition of the uptake rate factor $k_F(C_S)$, which clearly demonstrates the deviation from first-order kinetics. Eq. (7) was fit to the data in Fig. 6 using k_1, k_2 and J_0 as

fitting parameters. The data fitting procedure included the overlapping data points (points from multiple C_0 overlapping over portions of their corresponding C_S ranges), along with the standard deviation of U_R (shaded bands in Fig. 6). The inclusion of the standard deviation of U_R in the data fitting places stronger weighting on data points having the least uncertainty. R^2 for astrocytes and GBM43 cells are 0.997 and 0.985, respectively. The extracted values of k_1, k_2 and J_0 are presented in Table 2 for astrocytes and GBM43 cells.

**Table 2** Kinetic parameters extracted from experimental data

	k_1 (10^{-12} L s^{-1} cell^{-1})	k_2 (μM)	J_0 (fmol s^{-1} cell^{-1})
Astrocytes	0.87 ± 0.007	46 ± 0.8	0.09 ± 0.002
GBM43	2.3 ± 0.03	13 ± 1.3	0.06 ± 0.003

Fig. 7 magnifies the low C_S range (0-100 μM) of Fig. 6 to illustrate more clearly the non-linearity of U_R vs. C_S and the transition from a regime in which both terms contribute strongly to a regime in which the linear term dominates. In Fig. 7 , solid lines labeled as 'Kinetic Model Fit' are the same curves shown in Fig. 6 , and solid lines labeled as 'linear' and 'MM' represent the linear and MM terms from Eq. (7) using the corresponding values from Table 2. These linear and MM curves quantify the contribution of each mechanism to the measured U_R at any given C_S. The crossover point between linear and MM curves indicates the concentration at which both mechanisms contribute equally. The crossover points occur at 13 and 55 μM for GBM43 and astrocytes, respectively, mainly due to the fact that the linear term (k_1) is 2.5 times larger in GBM43 than in astrocytes (see Table 2). In the low concentration range (0–20 μM), which corresponds to the extracellular H_2O_2 concentration associated to the homeostatic level,[6,100] GBM43 and astrocytes exhibit contribution ratios of approximately 1:1 and 2:1 (MM:linear), respectively. As the concentration increases the MM mechanism reaches saturation and the linear mechanism takes over the MM mechanism. The MM saturation value (J_0) in GBM43 is 66.6% of that in astrocytes.

To illustrate how U_R–C_S deviates from first order as C_S increases, dashed lines in Fig. 7 show linear extrapolations of the initial slopes in the data curves, obtained from linear regressions of the experimental data of U_R–C_S in the range of 0–20 μM H_2O_2. These linear regressions yielded k_F of $(2.63 \pm 0.005) \times 10^{-12}$ L s^{-1} cell^{-1} for human astrocytes and $(4.2 \pm 0.02) \times 10^{-12}$ L s^{-1} cell^{-1} for GBM43, which are comparable to results from typical volumetric measurements,[27] as discussed in Section 4.

3.5 Simulation of the 2D cell cultures based on the determined parameters

The kinetic parameters k_1, k_2 and J_0 in Table 2 are included in the numerical solution of a diffusion–reaction system representing the same geometry of the 2D cell culture. For a given cell type, simulations are performed at various C_0 while keeping the values of k_1, k_2 and J_0 fixed. Simulated curves of C_S and G_S versus time are indicated by dashed lines in Figs. 4 and 5, respectively. The simulation captures the qualitative features of the experimental curves, including decreasing slopes with increasing time, relative changes in C_S and G_S at long times for various values of C_0
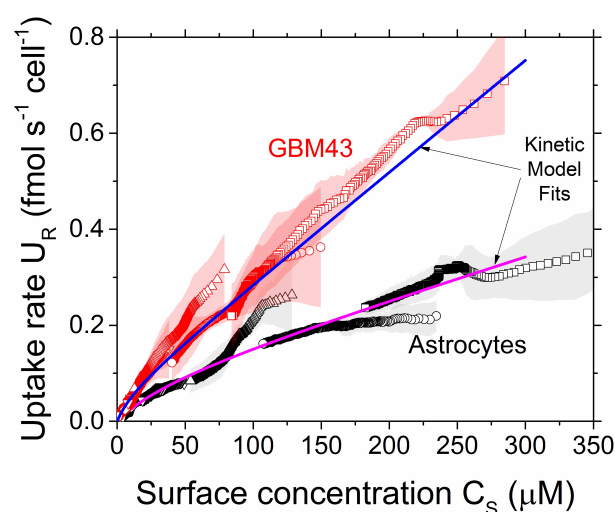
Fig. 6 The uptake rate of H_2O_2, U_R, as a function of surface concentration, C_S, for astrocytes and GBM43 as measured experimentally (symbols) and as obtained from the best fits to a kinetic model (solid lines) that considers linear and Michaelis-Menten components. U_R is computed as the experimental surface flux, F_S, divided by the cell density. Shaded bands indicate standard deviation of the mean of U_R from triplicate experiments. For each cell type, results are presented for C_0 of 500 (squares), 300 (circles), 200 (up-triangles), 100 (down-triangles), 60 (rhombuses) and 20 μM (pentagons); within each experiment at a given C_0, C_S evolves from high concentration (short time) to low concentration (long time).

and the relative differences between behavior of astrocytes and GBM43. The simulation did not include effects such as natural convection[10] and potential mixing effects due to the MEA chip motion at 300 s, which would result in a better fit to the data but would require assumptions regarding the magnitudes of these effects. Compared to simulations with the constant k_F extracted at low H_2O_2 concentrations (0–20 μM), the simulated curves using the kinetic parameters in Table 2 better capture the main features of the uptake mechanisms of astrocytes and GBM43 cells over the investigated range of C_S and over a larger time window (see Fig. S-9†).

4 Discussion

In this study we have demonstrated the analytical capabilities of the MEA approach to measure cellular uptake kinetics in real time. It is informative to compare the results from the current study with those from prior experiments. In typical volumetric experiments,[15,23,24,101–104] a first-order rate coefficient k_{obs} (in units of s^{-1}) is obtained from

$$\frac{dC_{vol}}{dt} = k_{obs}C_{vol} \tag{8}$$

where C_{vol} is the volumetric concentration. As discussed by Wagner et. al.,[24] the value of k_{obs} is dependent on both the solution volume (V) and number of cells (N), but normalization by N and V yields a rate constant k_{cell}, in units of L s^{-1} cell^{-1}, which can be directly compared for various experiments.

$$k_{cell} = \frac{V}{N}k_{obs} \tag{9}$$
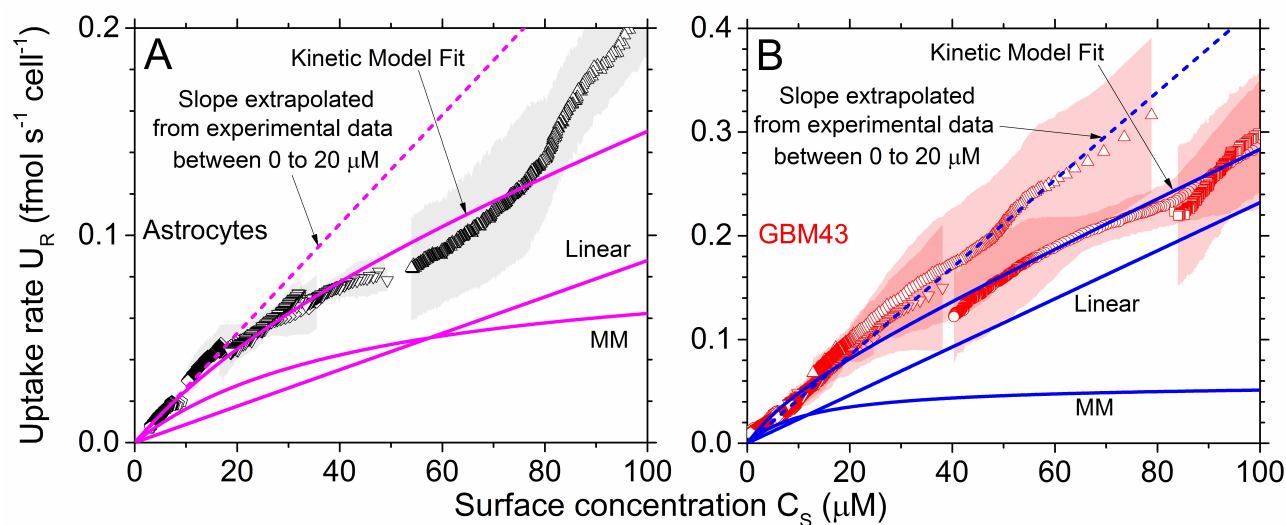
Fig. 7 The uptake rate, U_R, as a function of the surface concentration, C_S, over the low concentration range for astrocytes (A) and GBM43 (B). Experimental data points (symbols) and solid lines labeled as "Kinetic Model Fit" are the same as in Fig. 6, and the same symbols are used to indicate initial concentrations. Shaded bands indicate standard deviation of the mean of U_R from triplicate experiments. Linear and Michaelis-Menten (MM) kinetic components are indicated by solid lines which are labeled accordingly, illustrating the relative magnitudes and the cross-over point of the two terms. Dashed lines extrapolate the slope from experimental data within 0–20 μM in order to predict uptake rates at higher concentration range based on the conventional first-order kinetics approach.

The uptake rate factor k_F, defined earlier as the ratio U_R/C_S, allows quantitative comparison of MEA results to k_{cell} or k_{obs} from volumetric measurements, independent of diffusion geometry and mass transport. Based on Figs. 6 and 7, it is clear that k_F varies with C_S; the units for U_R and C_S in these figures have been chosen in order to provide k_F in the same units as k_{cell} (L s^{-1} cell^{-1}). In addition to this concentration-dependence, differences between k_F values from MEA measurements and k_{cell} values from volumetric measurements are expected due to differences in cell geometry (i.e., adherent versus suspended) and different relationships between C_S and C_{vol} associated with the hydrodynamics (i.e., static versus stirred solution). In experiments involving adherent cells in stirred solutions or suspended cells, $C_S \approx C_{vol}$ and Eq. (8) is the governing equation, so volumetric measurements yield k_{cell} values corresponding to C_0, if sampled within a short period after exposing the cells to C_0. By considering a number of C_0 values, such techniques have been used to study the concentration-dependence of k_{cell}.[28–32] In contrast, experiments involving adherent 2D cultures exposed to analyte in unstirred solution for specific intervals, followed by stirring just prior to volumetric sampling, will have $C(z,t)$ (during the uptake period) comparable to that in the current study. In this class of experiments, the C_{vol} observed after an uptake period T_0 can be related to C_0, C_S and k_F via

$$C_{vol}(T_0) = C_0 - \frac{N}{V} \int_0^{T_0} k_F C_S(t)\,dt \qquad (10)$$

For small T_0, which is typical in this class of experiments, a semilogarithmic plot of C_{vol} vs. T_0 is approximately linear and k_{cell} is extracted from the slope of this curve. Since C_S is less than the concentration averaged throughout the volume, such experiments will yield k_{cell} values lower than k_F (obtained in this work) or lower than the k_{cell} values inferred from experiments governed by Eq. (8). These observations indicate that there are qualitative and quantitative differences between experiments, dictated by cell geometry (adherent or suspended) and hydrodynamics (stirred or unstirred).

In our experiments, values for k_F at low C_S were determined from the average slope of the U_R–C_S relationships in the range of $0 < C_S < 20$ μM (dashed curves in Fig. 7), yielding $k_F = (2.63 \pm 0.005) \times 10^{-12}$ L s^{-1} cell^{-1} for human astrocytes and $(4.2 \pm 0.02) \times 10^{-12}$ L s^{-1} cell^{-1} for GBM43. Using volumetric approaches with initial concentration of 20 μM, Doskey et. al. measured k_{cell} values (all in units of L s^{-1} cell^{-1}) between 4.4×10^{-12} and 7.3×10^{-12} for human astrocytes, 4.8×10^{-12} for GBM U87, and 4.6×10^{-12} for GBM U118.[27] Compared to Doskey et. al., our values of k_F are in the same range, although the smaller value for astrocytes relative to that for GBM43 is in opposition to the general trend of tumor cells having lower k_{cell} than normal cells.[27] Since this trend may invert itself at higher concentrations, as indicated by Makino et. al.,[32] characterization over a wider range of surface concentrations is warranted if H_2O_2 is going to be used as a therapeutic agent against cancer.

The concentration dependence of U_R can also be compared to prior volumetric studies. The biphasic behavior in U_R–C_S is comparable to that reported by Makino et. al. in studies on rat astrocytes and C6 glioma using 2D cell cultures in stirred media.[28–32] These studies attributed the linear behavior to catalase (CAT) and the Michaelis-Menten behavior to glutathione peroxidase (GPx1).[32,105–107] Two observations are evident between our results for human cells and those of Makino et. al. for rat cells. First, Makino et. al. observed that C6 glioma cells exhibit a higher U_R compared to astrocytes for concentrations above 20 μM, but

a lower rate between 0-20 μM.[32] In contrast, our results show higher U_R in GBM43 than in astrocytes over the entire investigated concentration range (0–350 μM). Second, the ratio of J_0 for cancer to normal cells in Makino et. al. is 1.76 whereas that ratio in our results is 0.67.[32] Based on various issues which have been raised regarding the use of rat C6 glioma as a model for human glioblastoma and comparisons regarding growth, invasion, metastasis and drug response,[108–110] differences are expected between human and rat cells. For human cells, biochemical analyses indicate that glioblastoma contains more CAT but less GPx1 than astrocytes;[111] assuming the correlation by Makino et. al.[28] wherein the linear and MM mechanisms correspond to CAT and GPx1, respectively, our results are in qualitative agreement with that report.

The U_R–C_S relationships shown in Figs. 6 and 7 consist of sets of overlapping time trajectories, obtained using various C_0 values. For each cell type, these trajectories can provide insights into the relative effects of cumulative exposure to the analyte, e.g. by comparing the behavior at long exposure times for a large C_0 with that at short time for a smaller C_0. Such time-dependence could be used to quantify the onset of toxicity in prior studies.[15,112] In the current experiment, the trajectories for GBM43 show a tail-off in U_R after long exposure, i.e., the U_R values fall below those extrapolated from the intermediate-time regime. Such a roll-off could be indicative of H_2O_2 toxicity or reduction in H_2O_2 scavenging ability. In the case of astrocytes, comparable roll-off is not observed. Although clear changes in morphology were observed for both cell types after exposure to 300 and 500 μM H_2O_2 (see Fig. S-4†), the roll-off in U_R was moderate even for the GBM43 cells. The continuous monitoring of C_S over the course of the experiment allows a more accurate determination of the cumulative exposure of the cells to the analyte, in comparison to experiments in unstirred solutions followed by volumetric sampling.

The MEA approach should be well-suited to assess the chemical impact of one cell type on others when multiple cell types are cultured together (i.e., co-cultured). Studies have shown that the chemical microenvironment differs significantly among 2D cultures containing one, two and three different cell types cultured together,[113] and these observations have been ascribed to paracrine signaling via cell secreted factors.[9–11,114] Seeding of various cell types on a surface using cell patterning techniques[115] followed by co-culture could be used to measure kinetic parameters under the influence of paracrine signaling. The MEA approach allows measurements in unstirred solution, preserving the natural diffusion environment, and can in principle provide information on spatial heterogeneity, e.g., by localizing at the cell type of interest. Once the kinetic parameters are determined, they can be incorporated into 3D models to study the behavior of cells within tissue.

The MEA approach could be applied for other electroactive species without major adjustments and provides customizable spatial and temporal resolutions. Although the focus of the present study is on H_2O_2, the same MEA and methodology, except for minor adjustment of bias potential, can be used to measure uptake kinetics and C_S of other electroactive species of biological interest including dopamine and serotonin. The current

experiment utilized platinum electrodes, which yielded relatively high sensitivity but also a relatively long time for stabilization of the H_2O_2 response.[116–121] The latter dictated a waiting period of 300 s between addition of H_2O_2 and start of concentration measurements. Other materials, e.g., carbon electrodes, could reduce the electrode stabilization time, but trade-offs in sensitivity are expected.[117–121] As shown elsewhere,[81] parameters such as sampling period and spatial resolution can be customized to fit other requirements, e.g., sub-second transient concentrations and gradients have been measured with sampling period of 10 ms and inter-electrode distance of 35 μm.

5 Conclusions

In this work, we demonstrate the use of a MEA customized for typical 2D culture setups to measure dynamic H_2O_2 concentration profiles from normal (human astrocytes) versus astrocyte derived cancer (GBM43) cells. The MEA provides multi-point concentration data with a sampling period of 0.5 s. At each time point, the concentration data is fit using an analytical expression for a 1D diffusion/reaction system, allowing extrapolation of the surface concentration and surface gradient. Measurements at various initial concentrations allow determination of the uptake rate over a wide range of surface concentrations. Both cell types show surface concentration dependent uptake rates, i.e., non-linear kinetics. The results show that GBM43 cells have increased H_2O_2 uptake rates as compared to astrocytes due primarily to an elevated linear scavenging mechanism, which has previously been attributed to catalase. The Michaelis-Menten components are comparable for the two cell types for H_2O_2 concentrations within the 0–100 μM range. A comparison of the diffusion–reaction models using the non-linear parameters and standard first-order relationships indicates that the overall behavior is better described by the non-linear relationships. As shown in Eq.(10) and associated discussion, our results can also be used to quantitatively understand the differences between volumetric measurements using stirred versus unstirred media during uptake.

The monitoring of U_R vs C_S can also be used to quantify cumulative exposure effects, e.g., by comparing the uptake rate observed at the same C_S for different initial concentrations and therefore different cumulative exposures to H_2O_2. In the current experiment, a tail-off in uptake rate after long exposure to high concentrations of H_2O_2 is observed for GBM43 cells. The capabilities to quantify cumulative exposure effects and uptake rates over a wide range of cell surface concentrations are relevant for both toxicity studies and evaluation of potential therapeutic approaches based on differential uptake by cancerous versus normal cells.

In addition to shedding light on mechanistic behavior, the resulting kinetic parameters should be well suited for developing reaction–diffusion models that more accurately describe more complex culture/tissue geometries. Key aspects include measurements in a more natural local environment and the ability to obtain U_R vs C_S relationship which are nominally independent of the specific diffusion geometry. The MEA technique can also be extended to mixed cultures and multi-analyte measurements, e.g., monitoring of both uptaken and released analytes. Collectively,

these capabilities can provide parameters which, when coupled with a diffusion model representing a realistic geometry for influx/efflux of various analytes, can yield models which more accurately represent the behavior of 3D cultures and tissue microenvironments.

Conflicts of interest

There are no conflicts of interest to declare.

Acknowledgements

References

1 C. C. Winterbourn, *Nature chemical biology*, 2008, **4**, 278.

2 A. C. von Eschenbach, *Nature Reviews Cancer*, 2004, **4**, 820.

3 H. J. Forman, *Free Radical Biology and Medicine*, 2007, **42**, 926–932.

4 B. C. Dickinson and C. J. Chang, *Nature chemical biology*, 2011, **7**, 504.

5 H. S. Marinho, C. Real, L. Cyrne, H. Soares and F. Antunes, *Redox Biology*, 2014, **2**, 535 – 562.

6 F. Antunes and P. M. Brito, *Redox biology*, 2017, **13**, 1–7.

7 H. Link, D. Christodoulou and U. Sauer, *Current opinion in biotechnology*, 2014, **29**, 8–14.

8 R. Benfeitas, M. Uhlen, J. Nielsen and A. Mardinoglu, *Frontiers in cell and developmental biology*, 2017, **5**, 65.

9 A. L. Paguirigan and D. J. Beebe, *BioEssays*, 2008, **30**, 811–821.

10 H. Yu, I. Meyvantsson, I. A. Shkel and D. J. Beebe, *Lab on a Chip*, 2005, **5**, 1089–1095.

11 F. Guo, J. B. French, P. Li, H. Zhao, C. Y. Chan, J. R. Fick, S. J. Benkovic and T. J. Huang, *Lab on a Chip*, 2013, **13**, 3152–3162.

12 B. P. Dranka, G. A. Benavides, A. R. Diers, S. Giordano, B. R. Zelickson, C. Reily, L. Zou, J. C. Chatham, B. G. Hill, J. Zhang *et al.*, *Free Radical Biology and Medicine*, 2011, **51**, 1621–1635.

13 B. Chance, H. Sies and A. Boveris, *Physiological reviews*, 1979, **59**, 527–605.

14 J. R. Stone and S. Yang, *Antioxidants & redox signaling*, 2006, **8**, 243–270.

15 M. Gülden, A. Jess, J. Kammann, E. Maser and H. Seibert, *Free Radical Biology and Medicine*, 2010, **49**, 1298–1305.

16 C. Röhl, E. Armbrust, E. Herbst, A. Jess, M. Gülden, E. Maser, G. Rimbach and C. Bösch-Saadatmandi, *Neurotoxicity research*, 2010, **17**, 317–331.

17 K. J. Barnham, C. L. Masters and A. I. Bush, *Nature reviews Drug discovery*, 2004, **3**, 205.

18 L. C. Seaver and J. A. Imlay, *J. Bacteriol.*, 2001, **183**, 7182–7189.

19 L. E. Tomalin, A. M. Day, Z. E. Underwood, G. R. Smith, P. Dalle Pezze, C. Rallis, W. Patel, B. C. Dickinson, J. Bähler, T. F. Brewer *et al.*, *Free Radical Biology and Medicine*, 2016, **95**, 333–348.

20 S. Desagher, J. Glowinski and J. Premont, *Journal of Neuroscience*, 1996, **16**, 2553–2562.

21 S. Desagher, J. Glowinski and J. Prémont, *Journal of Neuroscience*, 1997, **17**, 9060–9067.

22 F. Antunes and E. Cadenas, *FEBS Letters*, 2000, **475**, 121–126.

23 R. Dringen, P. G. Pawlowski and J. Hirrlinger, *Journal of neuroscience research*, 2005, **79**, 157–165.

24 B. A. Wagner, J. R. Witmer, T. J. van't Erve and G. R. Buettner, *Redox Biology*, 2013, **1**, 210–217.

25 B. K. Huang and H. D. Sikes, *Redox biology*, 2014, **2**, 955–962.

26 A. Bagulho, F. Vilas-Boas, A. Pena, C. Peneda, F. C. Santos, A. Jerónimo, R. F. M. de Almeida and C. Real, *Redox Biology*, 2015, **6**, 454–460.

27 C. M. Doskey, V. Buranasudja, B. A. Wagner, J. G. Wilkes, J. Du, J. J. Cullen and G. R. Buettner, *Redox biology*, 2016, **10**, 274–284.

28 N. Makino, Y. Mochizuki, S. Bannai and Y. Sugita, *Journal of Biological Chemistry*, 1994, **269**, 1020–1025.

29 K. Sasaki, S. Bannai and N. Makino, *Biochimica et Biophysica Acta (BBA)-General Subjects*, 1998, **1380**, 275–288.

30 K. Hashida, Y. Sakakura and N. Makino, *Biochimica et Biophysica Acta (BBA)-General Subjects*, 2002, **1572**, 85–90.

31 N. Makino, K. Sasaki, K. Hashida and Y. Sakakura, *Biochimica et Biophysica Acta (BBA)-General Subjects*, 2004, **1673**, 149–159.

32 N. Makino, T. Mise and J.-i. Sagara, *Biochimica et Biophysica Acta (BBA)-General Subjects*, 2008, **1780**, 927–936.

33 L. Sokoloff, M. Reivich, C. Kennedy, M. Des Rosiers, C. S. Patlak, K. e. a. Pettigrew, O. Sakurada and M. Shinohara, *Journal of neurochemistry*, 1977, **28**, 897–916.

34 Y. Chen, N. E. Vartiainen, W. Ying, P. H. Chan, J. Koistinaho and R. A. Swanson, *Journal of neurochemistry*, 2001, **77**, 1601–1610.

35 A. Y. Shih, D. A. Johnson, G. Wong, A. D. Kraft, L. Jiang, H. Erb, J. A. Johnson and T. H. Murphy, *Journal of Neuroscience*, 2003, **23**, 3394–3406.

36 Y. Jiang and L. Uhrbom, *Upsala journal of medical sciences*, 2012, **117**, 113–121.

37 M. C. Papadopoulos and A. S. Verkman, *Nature Reviews Neuroscience*, 2013, **14**, 265.

38 A. Salazar-Ramiro, D. Ramírez-Ortega, V. Pérez de la Cruz, N. Y. Hérnandez-Pedro, D. F. González-Esquivel, J. Sotelo and B. Pineda, *Frontiers in immunology*, 2016, **7**, 156.

39 M. Rinaldi, M. Caffo, L. Minutoli, H. Marini, R. V. Abbritti, F. Squadrito, V. Trichilo, A. Valenti, V. Barresi, D. Altavilla, M. Passalacqua and G. Caruso, *International Journal of Molecular Sciences*, 2016, **17**, year.

40 D. Trachootham, J. Alexandre and P. Huang, *Nature Reviews*

Drug Discovery, 2009, **8**, 579–591.

41 C. M. Cabello, G. Wondrak *et al.*, *Current opinion in investigational drugs (London, England: 2000)*, 2007, **8**, 1022–1037.

42 S. Rodic and M. D. Vincent, *International Journal of Cancer*, 2018, **142**, 440–448.

43 H. S. Marinho, L. Cyrne, E. Cadenas and F. Antunes, *Methods Enzymol*, 2013, **526**, 159–173.

44 S. G. Rhee, T.-S. Chang, W. Jeong and D. Kang, *Molecules and cells*, 2010, **29**, 539–549.

45 M. B. Grisham, *Comparative Biochemistry and Physiology Part A: Molecular & Integrative Physiology*, 2013, **165**, 429 – 438.

46 H. Guo, H. Aleyasin, B. C. Dickinson, R. E. Haskew-Layton and R. R. Ratan, *Cell & Bioscience*, 2014, **4**, 64.

47 C. C. Winterbourn, *Biochimica et Biophysica Acta (BBA) - General Subjects*, 2014, **1840**, 730 – 738.

48 D. Dębski, R. Smulik, J. Zielonka, B. Michałowski, M. Jakubowska, K. Dębowska, J. Adamus, A. Marcinek, B. Kalyanaraman and A. Sikora, *Free Radical Biology and Medicine*, 2016, **95**, 323 – 332.

49 P. Lefrancois, V. S. R. Vajrala, I. B. Arredondo, B. Goudeau, T. Doneux, L. Bouffier and S. Arbault, *Phys. Chem. Chem. Phys.*, 2016, **18**, 25817–25822.

50 N. Baltes, L. Thouin, C. Amatore and J. Heinze, *Angewandte Chemie International Edition*, 2004, **43**, 1431–1435.

51 P. Sun, F. O. Laforge and M. V. Mirkin, *Physical Chemistry Chemical Physics*, 2007, **9**, 802–823.

52 S. Amemiya, A. J. Bard, F.-R. F. Fan, M. V. Mirkin and P. R. Unwin, *Annu. Rev. Anal. Chem.*, 2008, **1**, 95–131.

53 T. Sun, Y. Yu, B. J. Zacher and M. V. Mirkin, *Angewandte Chemie International Edition*, 2014, **53**, 14120–14123.

54 R. Chen, K. Hu, Y. Yu, M. V. Mirkin and S. Amemiya, *Journal of The Electrochemical Society*, 2016, **163**, H3032–H3037.

55 L. F. Jaffe and R. Nuccitelli, *J Cell Biol*, 1974, **63**, 614–628.

56 W. M. Kühtreiber and L. F. Jaffe, *The Journal of cell biology*, 1990, **110**, 1565–1573.

57 S.-K. Jung, J. R. Trimarchi, R. H. Sanger and P. J. Smith, *Analytical chemistry*, 2001, **73**, 3759–3767.

58 D. M. Porterfield, *Biosensors and Bioelectronics*, 2007, **22**, 1186–1196.

59 J. Shi, E. S. McLamore, D. Jaroch, J. C. Claussen, R. G. Mirmira, J. L. Rickus and D. M. Porterfield, *Analytical biochemistry*, 2011, **411**, 185–193.

60 E. McLamore, J. Shi, D. Jaroch, J. Claussen, A. Uchida, Y. Jiang, W. Zhang, S. Donkin, M. Banks, K. Buhman, D. Teegarden, J. Rickus and D. Porterfield, *Biosensors and Bioelectronics*, 2011, **26**, 2237 – 2245.

61 E. S. McLamore, S. Mohanty, J. Shi, J. Claussen, S. S. Jedlicka, J. L. Rickus and D. M. Porterfield, *Journal of Neuroscience Methods*, 2010, **189**, 14–22.

62 X. Liu, M. M. Ramsey, X. Chen, D. Koley, M. Whiteley and A. J. Bard, *PNAS*, 2011, **108**, 2668–2673.

63 S. M. Oja, Y. Fan, C. M. Armstrong, P. Defnet and B. Zhang, *Analytical Chemistry*, 2016, **88**, 414–430.

64 H. Meyer, H. Drewer, B. Gruendig, K. Cammann, R. Kakerow, Y. Manoli, W. Mokwa and M. Rospert, *Analytical Chemistry*, 1995, **67**, 1164–1170.

65 S.-Y. Liu, Y.-P. Chen, F. Fang, J. Xu, G.-P. Sheng, H.-Q. Yu, G. Liu and Y.-C. Tian, *Environmental Science & Technology*, 2009, **43**, 1160–1165.

66 K. Y. Inoue, M. Matsudaira, R. Kubo, M. Nakano, S. Yoshida, S. Matsuzaki, A. Suda, R. Kunikata, T. Kimura, R. Tsurumi *et al.*, *Lab on a Chip*, 2012, **12**, 3481–3490.

67 J. B. Wydallis, R. M. Feeny, W. Wilson, T. Kern, T. Chen, S. Tobet, M. M. Reynolds and C. S. Henry, *Lab Chip*, 2015, **15**, 4075–4082.

68 B. N. Kim, A. D. Herbst, S. J. Kim, B. A. Minch and M. Lindau, *Biosensors and Bioelectronics*, 2013, **41**, 736–744.

69 J. Rothe, M. Lewandowska, F. Heer, O. Frey and A. Hierlemann, *Journal of Micromechanics and Microengineering*, 2011, **21**, 054010.

70 J. Rothe, O. Frey, A. Stettler, Y. Chen and A. Hierlemann, *Analytical chemistry*, 2014, **86**, 6425–6432.

71 J. Wang, R. Trouillon, J. Dunevall and A. G. Ewing, *Analytical chemistry*, 2014, **86**, 4515–4520.

72 J. Wigström, J. Dunevall, N. Najafinobar, J. Lovrić, J. Wang, A. G. Ewing and A.-S. Cans, *Analytical chemistry*, 2016, **88**, 2080–2087.

73 J. Yan, V. A. Pedrosa, J. Enomoto, A. L. Simonian and A. Revzin, *Biomicrofluidics*, 2011, **5**, 032008.

74 M. Şen, K. Ino, K. Y. Inoue, T. Arai, T. Nishijo, A. Suda, R. Kunikata, H. Shiku and T. Matsue, *Biosensors and Bioelectronics*, 2013, **48**, 12–18.

75 J. Wang, R. Trouillon, Y. Lin, M. I. Svensson and A. G. Ewing, *Analytical chemistry*, 2013, **85**, 5600–5608.

76 H. Abe, K. Ino, C.-Z. Li, Y. Kanno, K. Y. Inoue, A. Suda, R. Kunikata, M. Matsudaira, Y. Takahashi, H. Shiku *et al.*, *Analytical chemistry*, 2015, **87**, 6364–6370.

77 C. Amatore, J. Delacotte, M. Guille-Collignon and F. Lemaître, *Analyst*, 2015, **140**, 3687–3695.

78 C. F. Lourenço, A. Ledo, J. Laranjinha, G. A. Gerhardt and R. M. Barbosa, *Sensors and Actuators B: Chemical*, 2016, **237**, 298–307.

79 F. Picollo, A. Battiato, E. Bernardi, A. Marcantoni, A. Pasquarelli, E. Carbone, P. Olivero and V. Carabelli, *Analytical chemistry*, 2016, **88**, 7493–7499.

80 W. Tedjo, J. Nejad, R. Feeny, L. Yang, C. Henry, T. Stuart and T. Chen, *Biosensors and Bioelectronics*, 2018, **114**, 78–88.

81 S. V. Sridharan, J. F. Rivera, J. K. Nolan, M. A. Alam, J. L. Rickus and D. B. Janes, *Sensors and Actuators B: Chemical*, 2018, **260**, 519 – 528.

82 M. G. Sullivan, H. Utomo, P. J. Fagan and M. D. Ward, *Analytical Chemistry*, 1999, **71**, 4369–4375.

83 X. Xu, S. Zhang, H. Chen and J. Kong, *Talanta*, 2009, **80**, 8 – 18.

84 R. Madangopal, M. Stensberg, M. Porterfield, J. Rickus and N. Pulliam, 2012 IEEE Sensors, 2012, pp. 1–4.

85 C. Amatore, S. Arbault, D. Bruce, P. de Oliveira, M. Erard and M. Vuillaume, *Faraday Discuss.*, 2000, **116**, 319–333.

86 C. Amatore, S. Arbault, D. Bruce, P. De Oliveira, M. Erard, N. Sojic and M. Vuillaume, *Analusis*, 2000, **28**, 506–517.

87 L. M. Kauri, S.-K. Jung and R. T. Kennedy, *Biochemical and biophysical research communications*, 2003, **304**, 371–377.

88 C. Amatore, S. Arbault, C. Bouton, K. Coffi, J.-C. Drapier, H. Ghandour and Y. Tong, *ChemBioChem*, 2006, **7**, 653–661.

89 V. Folmer, N. Pedroso, A. C. Matias, S. C. Lopes, F. Antunes, L. Cyrne and H. S. Marinho, *Biochimica et Biophysica Acta (BBA)-Biomembranes*, 2008, **1778**, 1141–1147.

90 D. Erudaitius, A. Huang, S. Kazmi, G. R. Buettner and V. G. Rodgers, *PloS one*, 2017, **12**, e0170442.

91 J. R. Liddell, C. Zwingmann, M. M. Schmidt, A. Thiessen, D. Leibfritz, S. R. Robinson and R. Dringen, *Journal of neuroscience research*, 2009, **87**, 2696–2708.

92 T. P. Szatrowski and C. F. Nathan, *Cancer Research*, 1991, **51**, 794–798.

93 U. E. Martinez-Outschoorn, Z. Lin, C. Trimmer, N. Flomenberg, C. Wang, S. Pavlides, R. G. Pestell, A. Howell, F. Sotgia and M. P. Lisanti, *Cell cycle*, 2011, **10**, 2504–2520.

94 D. Yan, H. Cui, W. Zhu, A. Talbot, L. G. Zhang, J. H. Sherman and M. Keidar, *Scientific reports*, 2017, **7**, 10831.

95 B. L. Carlson, J. L. Pokorny, M. A. Schroeder and J. N. Sarkaria, *Current protocols in pharmacology*, 2011, 14–16.

96 D. M. H. Kern, *J. Am. Chem. Soc.*, 1954, **76**, 4208–4214.

97 A. J. Bard and L. R. Faulkner, *Electrochemical Methods: Fundamentals and Applications*, Wiley, 2000.

98 L. Michaelis and M. L. Menten, *Biochem. Z*, 1913, **49**, 333–369.

99 K. A. Johnson and R. S. Goody, *Biochemistry*, 2011, **50**, 8264–8269.

100 H. Sies, *Redox Biology*, 2017, **11**, 613 – 619.

101 R. Dringen and B. Hamprecht, *Brain research*, 1997, **759**, 67–75.

102 R. Dringen, L. Kussmaul and B. Hamprecht, *Brain Research Protocols*, 1998, **2**, 223–228.

103 R. Dringen, L. Kussmaul, J. M. Gutterer, J. Hirrlinger and B. Hamprecht, *Journal of neurochemistry*, 1999, **72**, 2523–2530.

104 J. R. Liddell, S. R. Robinson and R. Dringen, *Neuroscience letters*, 2004, **364**, 164–167.

105 R. Dringen, *Progress in neurobiology*, 2000, **62**, 649–671.

106 R. Dringen, J. M. Gutterer and J. Hirrlinger, *The FEBS Journal*, 2000, **267**, 4912–4916.

107 R. Dringen, M. Brandmann, M. C. Hohnholt and E.-M. Blumrich, *Neurochemical research*, 2015, **40**, 2570–2582.

108 B. Grobben, P. De Deyn and H. Slegers, *Cell and Tissue Research*, 2002, **310**, 257–270.

109 S. Doblas, T. He, D. Saunders, J. Pearson, J. Hoyle, N. Smith, M. Lerner and R. A. Towner, *Journal of Magnetic Resonance Imaging*, 2010, **32**, 267–275.

110 A. Gieryng, D. Pszczolkowska, K. Bocian, M. Dabrowski, W. D. Rajan, M. Kloss, J. Mieczkowski and B. Kaminska, *Scientific reports*, 2017, **7**, 17556.

111 I. Dokic, C. Hartmann, C. Herold-Mende and A. Régnier-Vigouroux, *Glia*, 2012, **60**, 1785–1800.

112 M. C. Sobotta, A. G. Barata, U. Schmidt, S. Mueller, G. Millonig and T. P. Dick, *Free Radical Biology and Medicine*, 2013, **60**, 325–335.

113 M. C. Regier, E. T. Alarid and D. J. Beebe, *Integrative Biology*, 2016, **8**, 684–692.

114 L. Kim, Y.-C. Toh, J. Voldman and H. Yu, *Lab on a Chip*, 2007, **7**, 681–694.

115 F. Meiners, I. Plettenberg, J. Witt, B. Vaske, A. Lesch, I. Brand and G. Wittstock, *Analytical and bioanalytical chemistry*, 2013, **405**, 3673–3691.

116 Y. Zhang and G. S. Wilson, *Journal of Electroanalytical Chemistry*, 1993, **345**, 253–271.

117 S. B. Hall, E. A. Khudaish and A. L. Hart, *Electrochimica Acta*, 1998, **43**, 579–588.

118 S. B. Hall, E. A. Khudaish and A. L. Hart, *Electrochimica Acta*, 1998, **43**, 2015–2024.

119 S. B. Hall, E. A. Khudaish and A. L. Hart, *Electrochimica Acta*, 1999, **44**, 2455–2462.

120 S. B. Hall, E. A. Khudaish and A. L. Hart, *Electrochimica Acta*, 1999, **44**, 4573–4582.

121 S. B. Hall, E. A. Khudaish and A. L. Hart, *Electrochimica Acta*, 2000, **45**, 3573–3579.
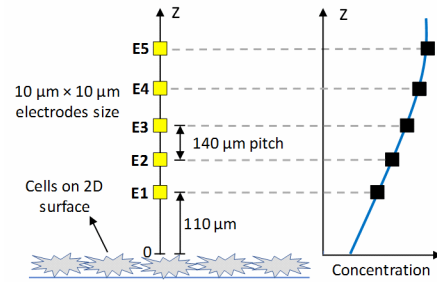
Reconstructed analyte concentration profile using 1D microelectrode array enables characterization of uptake kinetics vs. analyte concentration at the cell surface.